Supplementary Material: End-to-End Conformal Prediction for Trajectory Optimization

A. Details of the E2E-CP-IRA algorithm

The algorithm of E2E-CP using IRA at time t is delineated in Algorithm S1, and its flowchart is shown in Figure S.1. Note that at time $t = 0$, the input parameter $\alpha_{0:T}$ is initialized as $\alpha_0 = 0,\ \alpha_{1:T} = \alpha/T$, $\beta_{0:t-1}$ is omitted, and the posterior probability calculation in Line 4 is replaced by the assignment $\beta_0 = 0$. ϵ is a given small tolerance. At time t, the robot first obtains the current system state x_t and the joint obstacle states Y_t (Line 2). Then, based on the currently observed joint obstacle states $Y_0, ...Y_t$, the future joint obstacle states $\hat{Y}_{t+1|T}, ..., \hat{Y}_{T|t}$ are predicted using LSTMs (Line 3). Additionally, based on x_t and D^2_{cal}, the posterior collision risk can be calculated through (9) (Line 4). After initialization (Line 5), IRA jointly optimizes risk allocation and trajectory through iteration (Line 6-12). Specifically, in each iteration, IRA first computes the optimal control $u^n_{t:T-1}$, state $x^n_{t+1:T}$, and cost $J^*(\alpha^n_{t+1:T})$ for the current iteration based on the risk allocation $\alpha^n_{t+1:T}$ obtained from the previous iteration (Line 7). The active and inactive constraint sets $\mathcal{I}_{act},\ \mathcal{I}_{ina}$ are determined based on the optimal state $x^n_{t+1:T}$ (Line 8). And then, by sequentially applying the inactive constraint tightening (17) (Line 9) and the redundant risk reallocation (19) (Line 10), the updated risk allocation $\alpha^{n+1}_{t+1:T}$ is obtained. Finally, if the convergence condition is satisfied, the optimal control $u^{n-1}_{t:T-1}$ and the risk allocation $u^{n-1}_{t+1:T}$ are output; otherwise, the next iteration begins (Line 12).

Algorithm S.1 E2E-CP using IRA at time t

1: **Input:** α, $\alpha_{t:T}$, $\beta_{0:t-1}$, ϵ, η, D^1_{cal}, D^2_{cal}
2: Observe the system state x_t and joint obstacle states Y_t
3: $\hat{Y}_{t+1|t}, ..., \hat{Y}_{T|t} \leftarrow$ Trajectory prediction using LSTMs based on $Y_0, ..., Y_t$
4: $\beta_t \leftarrow$ Posterior probability calculation (9) ▷ Using x_t and D^2_{cal}
5: $J^*(\alpha^{-1}_{t+1:T}) \leftarrow \infty$, $\alpha^0_{t+1:T} \leftarrow \alpha_{t+1:T}$, $n \leftarrow 0$ ▷ Initialization of IRA
6: **repeat**
7: $\quad J^*(\alpha^n_{t+1:T}),\ x^n_{t+1:T},\ u^n_{t:T-1} \leftarrow$ Solve the lower-stage problem (12) with $\alpha^n_{t+1:T}$
8: $\quad \mathcal{I}_{act},\ \mathcal{I}_{ina},\ N_{act} \leftarrow$ Identification of active and inactive constraints
9: $\quad \widetilde{\alpha}^n_{t+1:T} \leftarrow$ Transitional risk allocation calculation (17)
10: $\quad \alpha^{n+1}_{t+1:T} \leftarrow$ New risk allocation calculation (19)
11: $\quad n \leftarrow n + 1$
12: **until** $|J^*(\alpha^{n-1}_{t+1:T}) - J^*(\alpha^{n-2}_{t+1:T})| < \epsilon$
13: **Output:** $\beta_{0:t}$, $u^{n-1}_{t:T-1}$, $\alpha_{t+1:T} = \alpha^{n-1}_{t+1:T}$

B. Simulations with additional baselines

We examine the quadrotor model (Dixit et al., 2023) with the following linear dynamics.

$$\begin{aligned} \ddot{x} &= g\theta & \ddot{y} &= -g\phi & \ddot{z} &= \tfrac{1}{m_Q}u_1 \\ \ddot{\phi} &= \tfrac{l_Q}{I_{xx}}u_2 & \ddot{\theta} &= \tfrac{l_Q}{I_{yy}}u_3 & \ddot{\psi} &= \tfrac{l_Q}{I_{zz}}u_4 \end{aligned} \tag{S1}$$

where $g = 9.81$ represents the gravitational acceleration, $m_Q = 0.65$ denotes the mass, and $l_Q = 0.23$ is the distance between the quadrotor and the rotor. $I_{xx} = 0.0075$, $I_{yy} = 0.0075$, and $I_{zz} = 0.013$ correspond to the area moments of inertia about the principle axes in the body frame. The states are the position and orientation with the corresponding velocities and rates — $(x, y, z, \dot{x}, \dot{y}, \dot{z}, \phi, \theta, \psi, \dot{\phi}, \dot{\theta}, \dot{\psi}) \in \mathbb{R}^{12}$. The control inputs u_1, u_2, u_3, u_4 correspond to the thrust force in the body frame and three moments. The system (S1) is discretized using the sampling time $\Delta = 0.125$, and the total time is set to $T = 20$. The objective is to control the quadrotor to reach the target point p_{tar} while navigating around $M = 3$

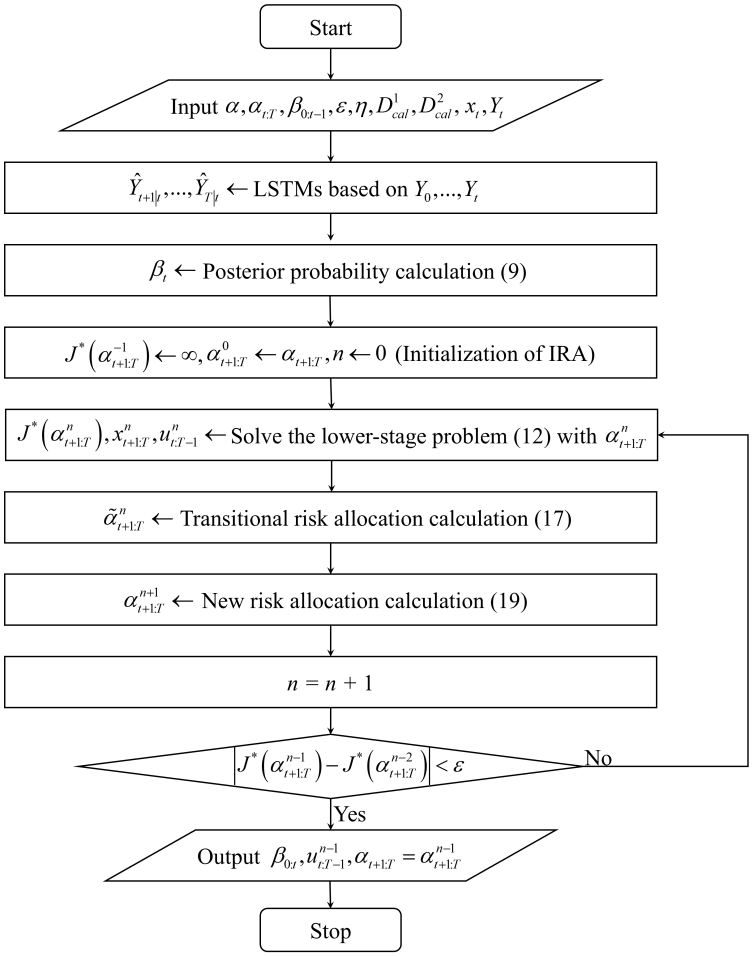

Figure S.1. Flowchart of Algorithm 1.

moving obstacles. We randomly generate 13,000 joint obstacle trajectories and randomly divide them into training D_{train}, calibration D_{cal}, and test D_{test} datasets with the set sizes 2,000, 10,000, and 1,000, respectively. We train an LSTM (Alahi et al., 2016) using D_{train} as the trajectory predictor. For the proposed E2E-CP, D_{cal} is further divided into D_{cal}^1 and D_{cal}^2 with sizes $|D_{cal}^1| = 2,000$ and $|D_{cal}^2| = 8,000$. We conduct 1,000 Monte Carlo simulations using D_{test}. The following state-of-art methods recently proposed in the literature are analyzed through 1,000 Monte Carlo simulations.

(i) Conformal Control (CC) proposed in Lekeufack et al. (2024).
(ii) ACI for Motion Planning (ACI-MP) proposed in Dixit et al. (2023).
(iii) Recursively Feasible MPC using CP (RF-CP) proposed in Stamouli et al. (2024)
(iv) Sequential CP (S-CP) proposed in Lindemann et al. (2023). Computation of the CP region and TO is performed sequentially.
(v) E2E-CP with ARA (E2E-CP-ARA): The method based on E2E-CP using average risk allocation.
(vi) E2E-CP with IRA (E2E-CP-IRA): The method based on E2E-CP using iterative risk allocation.

Table S.1 shows the average cost, average computation time, and collision avoidance rate of 1,000 simulations using the quadrotor model with different methods. Benefiting from the feedback information of posterior probabilities, the average cost of E2E-CP-ARA shows a reduction of at least 11.35% compared to S-CP. Furthermore, by flexibly allocating the allowable risk provided by posterior probabilities, the average cost of E2E-CP-IRA exhibits a significant reduction compared with S-CP. Since the calculation of posterior probabilities does not incur additional computational burden, the average computation time of E2E-CP-ARA is essentially comparable to that of S-CP. Additionally, since CC and ACI-MP fail to fully utilize the information in the calibration dataset, they incur higher costs, which are 296% and 184% higher than

Table S.1. Average cost, computation time, and collision avoidance rate using the quadrotor model with different methods (η is the learning rate of CC).

		CC		ACI-MP	RF-CP	S-CP	E2E-CP	
							with ARA	with IRA
Average cost	$\eta = 1000$	59.248	$\alpha = 0.05$	17.970	15.794*	17.321	15.356	7.189
	$\eta = 500$	47.506	$\alpha = 0.10$	17.263	14.378*	16.168	14.228	6.798
	$\eta = 100$	22.459	$\alpha = 0.15$	16.096	11.922*	14.835	12.354	6.191
	$\eta = 50$	21.344	$\alpha = 0.20$	15.310	10.032*	13.217	10.222	5.398
Average computation time	$\eta = 1000$	0.019	$\alpha = 0.05$	0.022	0.487	0.022	0.027	0.038
	$\eta = 500$	0.019	$\alpha = 0.10$	0.026	0.494	0.020	0.021	0.039
	$\eta = 100$	0.021	$\alpha = 0.15$	0.021	0.545	0.021	0.020	0.037
	$\eta = 50$	0.022	$\alpha = 0.20$	0.022	0.500	0.020	0.019	0.036
Collision avoidance rate	$\eta = 1000$	97.0%	$\alpha = 0.05$	98.6%	98.7%	98.8%	98.2%	96.3%
	$\eta = 500$	92.8%	$\alpha = 0.10$	93.3%	96.9%	93.5%	94.6%	94.1%
	$\eta = 100$	82.5%	$\alpha = 0.15$	91.5%	92.4%	92.0%	90.2%	91.9%
	$\eta = 50$	79.1%	$\alpha = 0.20$	87.9%	90.0%	88.2%	86.7%	88.2%

* Until the value obtained after the TO problem converges, with the solving time far exceeding the sampling time (0.125s).

that of E2E-CP-IRA, respectively. Particularly for CC, it directly controls the collision avoidance rate by adjusting the weight of the collision penalty term in the objective function, which results in a higher average cost. However, it should be noted that, in practice, CC and ACI-MP are better suited for scenarios where the test data exhibit distribution shift, rather than the setup considered in this section. For RF-CP, thanks to the proposed normalized nonconformity score, its average cost is comparable to that of E2E-CP-ARA, but it remains 85.8% higher than E2E-CP-IRA. However, the normalized nonconformity score introduces mixed-integer variables into the TO problem, significantly increasing the computation time. As shown in Table S.1, the average computation time of RF-CP is more than an order of magnitude higher than that of E2E-CP-IRA and significantly exceeds the sampling time (0.125s), making it infeasible for real-time control. It is worth noting that the proposed framework can also be extended to use this normalized nonconformity score, as detailed in Section E.

C. Computation time of IRA and a hybrid method of ARA and IRA

Table S.2 shows the average computation time at each time t using the kinematic vehicle model with E2E-CP-IRA ($\alpha = 0.2$). It can be observed that, in practice, the majority of the additional computational burden introduced by IRA arises at the initial time $t = 0$, where it is used to obtain the initial risk allocation and initial trajectory. At subsequent time steps, by using the optimal solution from the previous time step (or iteration) as the initial value for the next time step (or iteration), the IRA algorithm can converge quickly. It is important to note that the TO problem at the initial time step can be solved offline, while the average computation time for TO at subsequent time steps is much smaller than the sampling time ($0.125s$). Therefore, E2E-CP-IRA is well-suited for real-time TO.

Table S.2. Average Computation Time (ACT) at each time t using the kinematic vehicle model with E2E-CP-IRA ($\alpha = 0.2$).

t	0 (offline)	1	2	3	4	5	6	7	8	9
ACT	2.3016	0.0348	0.0331	0.0316	0.0277	0.0255	0.0239	0.0220	0.0214	0.0217
t	10	11	12	13	14	15	16	17	18	19
ACT	0.0153	0.0110	0.0093	0.0086	0.0079	0.0070	0.0058	0.0050	0.0049	0.0019

Furthermore, we explore a hybrid method of ARA and IRA to achieve a trade-off between average cost and average computation time. Specifically, we define a switching time t_s, such that when $t < t_s$, the IRA method is used, and when $t \geq t_s$, the ARA method is applied. Table S.3 shows the average cost and computation time using the kinematic vehicle model with different switching time t_s ($\alpha = 0.2$). It can be observed that using IRA only at the initial time step results in

a 66.56% reduction in average cost. This is because the trajectory obtained at the initial time step determines the overall path of the entire trajectory. As t_s increases, the average cost naturally decreases. When t_s reaches 11, further increases in t_s no longer lead to significant reduction in the average cost. This is because, in our scenario, the interaction between obstacles and the vehicle is most intensive at the middle of the mission time. After $t > 11$, the obstacles and the vehicle have moved apart, significantly reducing the collision risk, which results in ARA and IRA optimizing nearly identical trajectory. Although the aforementioned hybrid method balances the trade-off between average cost and computation time, as previously mentioned, executing IRA at the initial time step is the primary source of both cost reduction and increased computation time.

Table S.3. Average cost and computation time using the kinematic vehicle model with different switching time t_s ($\alpha = 0.2$).

t_s	0 (ARA)	1	6	11	16	20 (IRA)
Average cost	15.13	5.06	3.74	2.90	2.89	2.89
Average computation time	0.078	0.118	0.121	0.129	0.129	0.131

D. Sensitivity analysis of the calibration set division

Table S.4 shows the average cost, average computation time and collision avoidance rate using the kinematic vehicle model and E2E-CP-ARA ($\alpha = 0.2$) with 10 different random calibration set divisions. Specifically, for each experiment, we randomly divide the calibration dataset D_{cal} into D^1_{cal} and D^2_{cal}. It can be observed that, for the ten random experiments, the standard deviation of the average cost is 0.643, and the coefficient of variation is 4.2%, indicating relatively low volatility. For the collision avoidance rate, its volatility is only 2.3%, and all values do not exceed the given tolerance (80%). Therefore, the proposed method is insensitive to the calibration set division.

Table S.4. Average cost, average computation time and collision avoidance rate using the kinematic vehicle model and E2E-CP-ARA ($\alpha = 0.2$) with 10 different random calibration set divisions.

Division index	1	2	3	4	5	6	7	8	9	10
Average cost	15.13	14.78	15.11	16.03	15.96	14.37	14.60	15.73	15.64	16.19
Average computation time	0.078	0.078	0.079	0.077	0.072	0.080	0.065	0.074	0.086	0.084
Collision avoidance rate	89.1%	89.2%	90.5%	88.2%	88.6%	88.4%	90.5%	89.2%	89.3%	89.9%

E. An extension using the normalized nonconformity score in Stamouli et al. (2024)

Stamouli et al. (2024) proposed a normalized nonconformity score, which can improve performance compared to S-CP (Lindemann et al., 2023). In this section, we incorporate this normalized nonconformity score into E2E-CP to further enhance its performance as follows. First, we still follow the content outlined prior to Section 4.1. Instead of using the original nonconformity score as in Section, we can redefine the nonconformity score at time τ as follows to replace (6).

$$\begin{aligned} R_\tau &= \max_{t=0,\dots,\tau-1} \left\{ \frac{\|Y_\tau - \hat{Y}_{\tau|t}\|}{\sigma_{\tau|t}} \right\} \\ R^{(i)}_\tau &= \max_{t=0,\dots,\tau-1} \left\{ \frac{\|Y^{(i)}_\tau - \hat{Y}^{(i)}_{\tau|t}\|}{\sigma_{\tau|t}} \right\} \quad \forall i = 1, ..., K \end{aligned} \tag{S2}$$

where

$$\sigma_{\tau|t} = \max_{j \in \mathcal{I}_{train}} \|Y^{(j)}_\tau - \hat{Y}^{(j)}_{\tau|t}\|, \quad \forall t,\ \tau > t \tag{S3}$$

where $\mathcal{I}_{train} = \{j : Y^{(j)} \in D_{train}\}$ denotes the set of indices of the data in the training set D_{train}. We note that, compared to the nonconformity score in Stamouli et al. (2024), we separate the nonconformity score at each time τ, which facilitates

the reallocation of the risk at each time step. Similarly, given an allocated risk α_τ for future time τ, the random variables $R_\tau, R_\tau^{(1)}, ..., R_\tau^{(K)}$ are exchangeable and the prediction region with coverage guarantee is derived according to Lemma 3.3 as follows.

$$\mathbb{P}\left\{\max_{t=0,\dots,\tau-1}\left\{\frac{\|Y_\tau - \hat{Y}_{\tau|t}\|}{\sigma_{\tau|t}}\right\} \leq C_\tau^{1-\alpha_\tau}\right\} \geq 1-\alpha_\tau \tag{S4a}$$

$$C_\tau^{1-\alpha_\tau} = Quantile_{1-\alpha_\tau}(R_\tau^{(1)}, ..., R_\tau^{(K)}, \infty) \tag{S4b}$$

Based on the $(1-\alpha_\tau)$-coverage prediction region defined in (S4a), the individual chance constraint $\mathbb{P}\{c(x_\tau, Y_\tau) \geq 0\} \geq 1-\alpha_\tau$ can be reformulated as the following lemma.

Lemma E.1. *(chance constraint) If Assumptions 3.1 and 3.2 hold, the constraint function c is L-Lipschitz continuous and $\max_{0\leq s\leq t}\{c(x_\tau, \hat{Y}_{\tau|t}) - LC_{\tau|t}^{1-\alpha_\tau}\} \geq 0$ is satisfied where $C_{\tau|t}^{1-\alpha_\tau} = \sigma_{\tau|t}C_\tau^{1-\alpha_\tau}$, then the individual chance constraint $\mathbb{P}\{c(x_\tau, Y_\tau) \geq 0\} \geq 1-\alpha_\tau$ is satisfied.*

Proof. According to the $(1-\alpha_\tau)$-coverage prediction region defined in S4a, we can obtain that

$$\mathbb{P}\left\{\bigcap_{t=0}^{\tau-1}\left\{\frac{\|Y_\tau - \hat{Y}_{\tau|t}\|}{\sigma_{\tau|t}}\right\} \leq C_\tau^{1-\alpha_\tau}\right\} \geq 1-\alpha_\tau \tag{S5}$$

According to that fact $t \leq \tau - 1$ and the definition, we have the following inequality.

$$\mathbb{P}\left\{\bigcap_{t=0}^{t}\left\{\|Y_\tau - \hat{Y}_{\tau|t}\| - C_{\tau|t}^{1-\alpha_\tau}\right\} \leq 0\right\} \geq \mathbb{P}\left\{\bigcap_{t=0}^{\tau-1}\left\{\|Y_\tau - \hat{Y}_{\tau|t}\| - C_{\tau|t}^{1-\alpha_\tau}\right\} \leq 0\right\} \geq 1-\alpha_\tau \tag{S6}$$

Based on (S6), we can further obtain the following inequality.

$$\mathbb{P}\left\{C_{\tau|s}^{1-\alpha_\tau} - \|Y_\tau - \hat{Y}_{\tau|s}\| \geq 0\right\} \geq 1-\alpha_\tau, \quad \forall s = 0, ..., t \tag{S7}$$

Note that the function c is L-Lipschitz continuous, the following inequality is obtained.

$$\|c(x_\tau, Y_\tau) - c(x_\tau, \hat{Y}_{\tau|t})\| \leq L\|Y_\tau - \hat{Y}_{\tau|t}\| \Longrightarrow c(x_\tau, Y_\tau) \geq c(x_\tau, \hat{Y}_{\tau|t}) - L\|Y_\tau - \hat{Y}_{\tau|t}\| \tag{S8}$$

If the constraint $\max_{0\leq s\leq t}\{c(x_\tau, \hat{Y}_{\tau|t}) - LC_{\tau|t}^{1-\alpha_\tau}\} \geq 0$ is satisfied, we have the following inequality.

$$\exists s = 0, ..., t \quad c(x_\tau, Y_\tau) \geq L(C_{\tau|s}^{1-\alpha_\tau} - \|Y_\tau - \hat{Y}_{\tau|s}\|) \tag{S9}$$

By combining (S7) and (S9), we ultimately obtain $\mathbb{P}\{c(x_\tau, Y_\tau) \geq 0\} \geq 1-\alpha_\tau$. □

Finally, it is sufficient to replace constraint (11e) in the TO problem (11) with $\max_{0\leq s\leq t}\{c(x_\tau, \hat{Y}_{\tau|t}) - LC_{\tau|t}^{1-\alpha_\tau}\} \geq 0$. For the posterior probability calculation and risk allocation method, since we have separated the nonconformity score at each time step τ, our proposed framework remains fully applicable. It is important to note that, as described in Section B, the constraint $\max_{0\leq s\leq t}\{c(x_\tau, \hat{Y}_{\tau|t}) - LC_{\tau|t}^{1-\alpha_\tau}\} \geq 0$ introduces mixed-integer variables into the TO problem, which significantly increases the solution time, especially when using the IRA method and dealing with nonlinear systems.

References

Alahi, A., Goel, K., Ramanathan, V., Robicquet, A., Fei-Fei, L., and Savarese, S. Social lstm: Human trajectory prediction in crowded spaces. In *Proceedings of the IEEE conference on computer vision and pattern recognition*, pp. 961–971, 2016.

Dixit, A., Lindemann, L., Wei, S. X., Cleaveland, M., Pappas, G. J., and Burdick, J. W. Adaptive conformal prediction for motion planning among dynamic agents. In *Learning for Dynamics and Control Conference*, pp. 300–314. PMLR, 2023.

Lekeufack, J., Angelopoulos, A. N., Bajcsy, A., Jordan, M. I., and Malik, J. Conformal decision theory: Safe autonomous decisions from imperfect predictions. In *2024 IEEE International Conference on Robotics and Automation (ICRA)*, pp. 11668–11675. IEEE, 2024.

Lindemann, L., Cleaveland, M., Shim, G., and Pappas, G. J. Safe planning in dynamic environments using conformal prediction. *IEEE Robotics and Automation Letters*, 2023.

Stamouli, C., Lindemann, L., and Pappas, G. Recursively feasible shrinking-horizon mpc in dynamic environments with conformal prediction guarantees. In *6th Annual Learning for Dynamics & Control Conference*, pp. 1330–1342. PMLR, 2024.